Helical spin waves, magnetic order, and fluctuations in the langasite compound $Ba_3NbFe_3Si_2O_{14}$

C. Stock,[1,2,*] L. C. Chapon,[3] A. Schneidewind,[4] Y. Su,[5] P. G. Radaelli,[6] D. F. McMorrow,[7]
A. Bombardi,[8] N. Lee,[9] and S.-W. Cheong[9]

[1]*NIST Center for Neutron Research, 100 Bureau Drive, Gaithersburg, Maryland 20899, USA*
[2]*Indiana University Cyclotron Facility, 2401 Milo B. Sampson Lane, Bloomington, Indiana 47404, USA*
[3]*ISIS Facility, Rutherford Appleton Laboratory, Chilton, Didcot OX11 0QX, United Kingdom*
[4]*Joint Research Group HZB–TU Dresden, Helmholtz-Zentrum fur Materialien und Energie, D-85747 Garching, Germany*
[5]*Juelich Centre for Neutron Science, IFF, Forschungszentrum Juelich, Outstation at FRM II, Lichtenbergstr. 1, D-85747 Garching, Germany*
[6]*Oxford Physics, Clarendon Laboratory, Parks Road, Oxford OX1 3PU, United Kindom*
[7]*London Centre for Nanotechnology, Department of Physics and Astronomy, University College London, London WC1E 6BT, United Kingdom*
[8]*Diamond Light Source Ltd., Harwell Science and Innovation Campus, Didcot, Oxfordshire OX11 0DE, United Kingdom*
[9]*Rutgers Center for Emergent Materials and Department of Physics and Astronomy, Rutgers University, 136 Frelinghuysen Road, Piscataway, New Jersey 08854, USA*

(Received 21 July 2010; revised manuscript received 25 January 2011; published 30 March 2011)

We have investigated spin fluctuations in the langasite compound $Ba_3NbFe_3Si_2O_{14}$ both in the ordered state and as a function of temperature. The low-temperature magnetic structure is defined by a spiral phase characterized by magnetic Bragg peaks at $\vec{q} = (0,0,\tau \sim 1/7)$ onset at $T_N = 27$ K as previously reported by Marty *et al.* [Phys. Rev. Lett. **101**, 247201 (2008)]. The nature of the fluctuations and temperature dependence of the order parameter is consistent with a classical second-order phase transition for a two-dimensional triangular antiferromagnet. We show that the physical properties and energy scales including the ordering wave vector, Curie-Weiss temperature, and spin waves can be explained through the use of only symmetric exchange constants without the need for a dominant Dzyaloshinskii-Moriya interaction. This is accomplished through a set of "helical" exchange pathways along the *c* direction imposed by the chiral crystal structure and naturally explains the magnetic diffuse scattering, which displays a strong vector chirality up to high temperatures, well above the ordering temperature. This illustrates a strong coupling between magnetic and crystalline chirality in this compound.

DOI: 10.1103/PhysRevB.83.104426 PACS number(s): 75.30.Ds, 75.30.Et, 75.30.Kz

I. INTRODUCTION

In geometrically frustrated magnets, each spin cannot satisfy all pairwise interactions as a result of the crystal symmetry and, therefore, remain disordered to temperatures well below the Curie-Weiss temperature (Θ_{CW}) where magnetic order is expected.[1–3] The simplest geometrically frustrated system is arguably the two-dimensional triangular lattice where all interactions cannot be satisfied, resulting in large degeneracies.[4]

Low-spin (or quantum) triangular antiferromagnets with $S \leqslant 1$ do not show long-range magnetic order because of the combination of strong quantum fluctuations and geometrical frustration and a number of interesting phases have been observed and proposed including resonating valence bond states and spin liquids.[5] Examples of low-dimensional triangular antiferromagnets include Cs_2CuCl_4 ($S = 1/2$), κ-(BEDT-TTF)$_2$Cu$_2$(CN)$_3$ ($S = 1/2$), $ZnCu_3(OH)_6Cl_2$ (Kagome), and $NiGa_2S_4$ ($S = 1$).[6–10] All of these systems display anomalous magnetic properties well below Θ_{CW} and illustrate the dramatic effects that crystal symmetry imposed degeneracy, or geometric frustration, can have on magnetic structures and excitations.

Large-S systems are interesting to investigate, as quantum fluctuations are completely suppressed and therefore reveal only the classical effects of frustration. An interesting example is the case of the anisotropic triangular lattice α-$NaMnO_2$, where the $S = 2$ spins, with dominant nearest-neighbor coupling, relieve the effects of frustration by reducing the dimensionality and behave like one-dimensional chains.[11] More complex systems include (Tb,Ho)MnO_3[12–14] and $RbFe(MoO_4)_2$,[15] where frustration results in spiral phases and coupling between magnetic and ferroelectric order parameters.[16] For some of these systems, the loss of inversion symmetry in the ordered magnetic state allows antisymmetric exchange (Dzyaloshinskii-Moriya interaction), which has been proposed to be very important to multiferroicity. It is therefore important to investigate the property of chirality and its relationship to the crystal structure, especially in systems that are noncentrosymmetric already in the paramagnetic state.[3]

An interesting class of compounds is the langasite series of materials, which consist of isolated triangular lattices (or trimers) on a hexagonal lattice. Attention to this system started with $La_3Ga_5SiO_{14}$ (LGS), which displays favorable piezoelectric properties and strong electromechanical coupling constants.[17] LGS has a $Ca_3Ga_2Ge_4O_{14}$-type structure with space group $P321$ and this structure type can accommodate a number of different cations, leading to a wide variety of different properties. For example, $Pr_3Ga_5SiO_{14}$ has drawn some attention as a two-dimensional Kagome system that magnetically orders only under chemical pressure.[18,19] The only langasite compounds discovered so far that display long-range magnetic order are those containing Fe^{3+} ions and have been observed to display a series of novel piezoelectric and magnetic properties.[20]

A particular iron-based langasite compound is $Ba_3NbFe_3Si_2O_{14}$, which consists of Fe^{3+} $S = 5/2$ ions. A detailed structural study of this compound has been

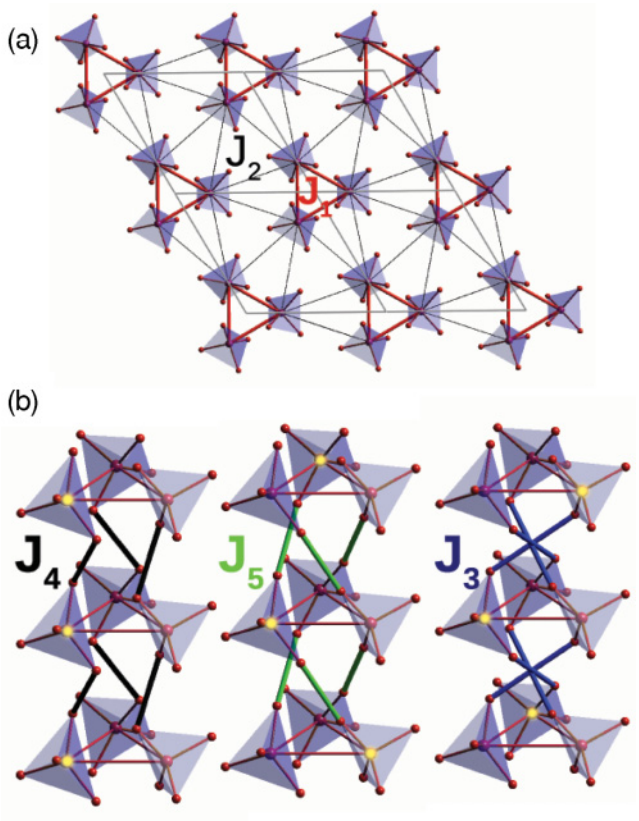

FIG. 1. (Color online) Crystal structure of $Ba_3NbFe_3Si_2O_{14}$ projected (a) in the *ab* plane and (b) along the *c* axis. FeO_4 tetrahedra are shown in light blue. Fe and O atoms are represented as large and small spheres, respectively. Ba, Nb, and Si atoms are omitted for clarity. Exchange interactions are shown in plane by thick lines (J_1) and thin lines (J_2). Along the *c* axis, the three inequivalent exchange interactions are marked by their respective O-O paths, shown as thick bonds. Fe atoms connected by the three exchange pathways are highlighted in yellow in (b).

presented previously illustrating a unique single-phase magnetic spiral structure, with each triangle adopting a conventional 120° arrangement but with a spiral pitch along the *c* axis resulting in a magnetic propagation vector of $q_0 = (0,0,1/7)$.[21] The underlying structure is displayed in Fig. 1. Figure 1(a) illustrates the Fe^{3+} framework in the *a*-*b* plane and shows that the material consists of triangles of magnetic ions arranged on a hexagonal lattice. Figure 1(b) illustrates the framework along the *c* axis. The space group is chiral and the crystal possess a handedness, as seen from the "helical" paths along the *c* axis [Fig. 1(b)]. The exchange pathways labeled $J_{i=1-5}$ are discussed later. The magnetic order occurs at $T_N = 27$ K despite a Curie-Weiss temperature of $\Theta_W = -173$ K, owing to the effects of low dimensionality and frustration. Further work on this material has suggested the possibility of multiferroic properties at low temperatures and as a function of an applied magnetic field.[20,22]

We present a neutron elastic and inelastic scattering study of the fluctuations and critical properties in $Ba_3NbFe_3Si_2O_{14}$. We show that the magnetic chirality is imposed by symmetric Heisenberg exchange only, without the need for a dominant Dzyaloshinskii-Moriya interaction, and illustrates a strong coupling between structural and magnetic chirality. The paper is divided into four sections discussing our results along with this Introduction and a section on the experimental details. We first investigate the temperature dependence of the magnetic correlations near the critical wave vector through the use of inelastic powder and single-crystal studies, to show that the transition behaves classically as expected for a two-dimensional triangular magnet. This section also includes our results using polarized neutrons to investigate the energy-integrated diffuse scattering as a function of temperature. To motivate our inelastic work, we then present our results from spin-dimer calculations that provide an estimate for the relative values of the magnetic exchange parameters. We then discuss the spin waves and our heuristic model to extract the exchange constants. We finish the paper with a derivation of the ordering wave vector and Curie-Weiss temperature. While Dzyaloshinskii-Moriya interactions are present owing to the symmetry of the lattice, we find that we can understand the ordering wave vector [$q_0 = (0,0,\sim 1/7)$], spin waves, and Curie-Weiss constant (Θ_{CW}) in terms of a model based solely on Heisenberg exchange with a magnetic chirality introduced because of the handedness forced by the crystal structure.

II. EXPERIMENTAL DETAILS

Neutron experiments utilized instruments at both the ISIS spallation neutron source (Rutherford Appleton Laboratory, UK) and the FRM2 reactor (Germany). To initially characterize the dynamics and temperature dependence, we used the MARI direct geometry chopper spectrometer at the ISIS facility. The sample consisted of 11 g of powder mounted in an annular geometry and cooled using a closed-cycle displex. A Gd Fermi chopper was used to define an incident energy in parallel with a disk chopper to suppress background and high-energy neutrons above ~250 meV. Fast neutrons, with energies in excess of ~1 eV, were removed using a nimonic (or t_0) chopper located close to the target face. To measure the magnetic fluctuations as a function of energy and temperature, we used a fixed incident energy of $E_i = 10$ meV taken with a Fermi chopper speed of 250 Hz.

The single-crystal sample, with a mass of 6 g, was grown using the floating-zone technique and was characterized at the test and alignment spectrometer at the ISIS facility using a four-circle geometry. The lattice constants were measured to be $a = b = 8.539$ Å and $c = 5.241$ Å, with $\gamma = 120°$. The sample was aligned such that Bragg reflections of the form (*H*0*L*) lay within the horizontal scattering plane. Two different sets of experiments were performed at the FRM2 reactor using a closed-cycle refrigerator to reach temperatures as low as 2.5 K. To measure the spin waves across the entire Brillouin zone, the PANDA cold triple-axis was used. A vertically focused pyrolytic graphite (PG002) monochromator was used to select an incident neutron energy reflected onto the sample position. A flat PG002 analyzer was used to select the final energy of the neutrons analyzed in the detector. A cooled beryllium filter on the scattered side filtered out higher order neutrons reflected off the monochromator and collimation sequence was set to open-80′-*S*-80′-open. Final energies of $E_f = 5.0$ and 2.5 meV were chosen to study the

low-energy spin waves and $E_f = 13.5$ meV was used to study the magnetic order parameter with the beryllium filter replaced by a graphite filter. All data taken on PANDA have been corrected for higher order contamination of the incident beam monitor that determines the counting time. The correction factor is discussed in detail elsewhere.[23,24]

To measure the energy-integrated diffuse magnetic scattering, we have used the DNS polarized, cold, two-axis diffractometer located at FRM2. An incident energy of 3.64 meV was selected using a horizontally and vertically focused PG002 monochromator. The beam was polarized using $m = 3$ Scharpf supermirror polarizers.[25] The polarization at the sample was fixed through the use of an xyz coil, with the x direction chosen to be parallel to the average $\vec{Q}$ at the sample position and z vertical. With the use of flipping coils in the incident and scattering beams, the two spin-flip and non-spin-flip cross sections could be measured with the neutron polarization along the three orthogonal Cartesian coordinates (a total of 12 channels). The flipping ratio was 20 ± 1 and was not found to deviate from this value regardless of the direction of neutron polarization. All spin-flip data have been corrected for the feed-through from the non-spin-flip channel. The scattered beam was measured with 24 detectors equally spaced 5° apart covering a total angular range in scattering angle (2θ) equal to 120°. These measurements were performed using a two-axis geometry and therefore provided an approximate measure of the energy-integrated intensity $[S(\vec{Q})]$.

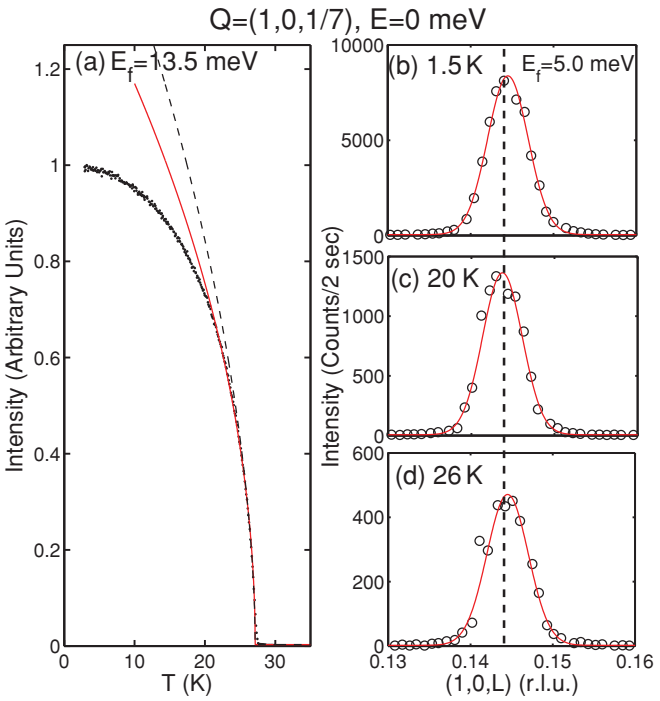

FIG. 2. (Color online) (a) Temperature dependence of the elastic magnetic scattering measured with a final energy of $E_f = 13.5$ meV taken on the PANDA cold triple-axis. Curves are power laws described in the text. (b–d) Scans along the (00L) direction illustrating that the incommensurability remains fixed with the temperature.

III. PARAMAGNETIC SCATTERING AND MAGNETIC ORDER

A. Magnetic order and wave vector

A summary of the elastic scattering that characterizes the magnetic structure is presented in Fig. 2 and illustrates the temperature dependence of the magnetic Bragg peak at $\vec{Q} = (1,0,\sim 1/7)$. The temperature dependence of the magnetic Bragg peak is plotted in Fig. 2(a) and was taken using the PANDA cold triple-axis with $E_f = 13.5$ meV. The solid (red) curve is a plot to a power law $I \propto (T_c - T)^{2\beta}$, with $T_c = 27$ K and $\beta = 0.25$, following the critical exponents measured in $CsMnBr_3$ and $CsVCl_3$.[34] Because the experiments were not optimized for the measurement of critical properties, we have chosen not to fit the critical exponents. Rather we have compared our data with the critical properties of other two-dimensional triangular magnets that are XY-like in nature and possess a 120° structure similar to that in one trimer in $Ba_3NbFe_3Si_2O_{14}$.

Figures 2(b)–2(d) illustrate scans along the (00L) direction at several temperatures. The results illustrate that while there is a significant change in the intensity, the wave vector of the magnetic peak does not change within error even close to the Neel transition temperature. This point contrasts with other incommensurate systems, where the incommensurability varies smoothly with temperature unless the transition is first order. For example, the field-driven commensurate-incommensurate transition in $CuGeO_3$ is first order and becomes second order on doping with nonmagnetic impurities such as Mg, resulting in a continuous change of the incommensurate wave vector near T_N.[26] Another example is the incommensurate transition in Rb_2ZnCl_4, which exhibits a strong temperature dependence of the wave vector near the critical temperature.[27] We now investigate the chirality using polarized neutrons, which is a measure of the order parameter.

B. Polarized diffuse scattering measurements

The spin of the neutron allows a sensitive measure of both the *phase* and the *magnitude* of the magnetic cross section. The cross sections for polarized neutrons have been studied theoretically and are presented in Refs. 29–32. Of particular interest is the spin-flip cross section when the incident beam is polarized parallel to the momentum transfer ($\vec{Q}$),

$$I^{+-/-+} = \sum_{ij} e^{i\vec{Q}\cdot(\vec{r}_i - \vec{r}_j)} p_i p_j^* \times [\vec{S}_{i\perp} \cdot \vec{S}_{j\perp} \mp i\hat{z} \cdot (\vec{S}_{i\perp} \times \vec{S}_{j\perp})]. \quad (1)$$

Here p is the magnetic scattering length and $S_\perp$ is the value of the magnetic spin perpendicular to the momentum transfer. The symbols $+-/-+$ denote the cross sections when scattering from a spin-up to a spin-down state and from a spin-down to a spin-up, respectively. In collinear magnets, the values of these cross sections are the same, as the second term in the Eq. (1) is identically 0.

In a chiral magnet, one can define a vector chirality via a vector product of two neighboring spins, averaged over three

spin pairs, by

$$\vec{\kappa} = \frac{2}{3\sqrt{3}} \sum_{i,j} [\vec{S}_i \times \vec{S}_j], \tag{2}$$

which is related to the cross product in the cross section written in Eq. (1). In a chiral magnet the cross product in Eq. (2) is not necessarily equal to 0, and I^{+-} is not equal to I^{-+}. This property of chiral magnets and polarized neutron scattering was first demonstrated in MnSi where the Dyzaloshinski-Moriya interaction results in spiral magnetic correlations.[33] Given that in our notation x is parallel to the average $\vec{Q}$, a subtraction of scattering channels in $+x$ and $-x$ channels gives the cross-product term above, sensitive to the chirality. The cross product in Eq. (1) does not appear when the incident beam polarization is perpendicular to the momentum transfer ($\vec{Q}$). This is the case for y and z polarizations and these two channels can be used to determine the magnetic moment direction or the orientation of $\vec{S}_\perp$ in Eq. (1).

Figure 3 provides an overview of the magnetic scattering cross section in the paramagnetic phase by displaying the spin-flip intensities for polarizations parallel to the three orthogonal directions x, y, and z at $T = 50$ K. A cut through the data along the (1,0,L) direction is plotted in Fig. 3(d) for the three polarizations. The spin-flip cross section parallel to x is a measure of the entire magnetic cross section. As illustrated in Fig. 3(d), the spin-flip cross section parallel to x is approximately twice that of the y and z channels. This

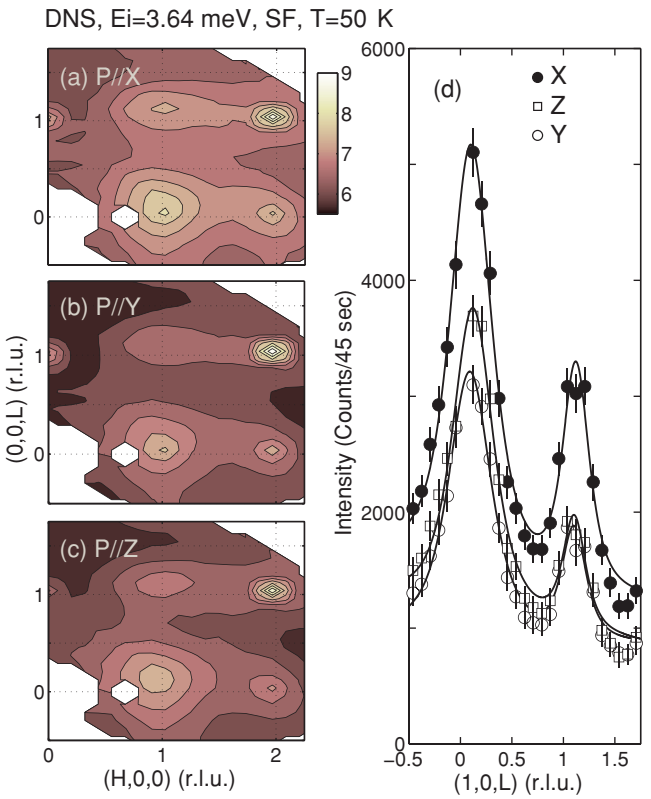

FIG. 3. (Color online) (a–c) The three spin-flip cross sections measured with the incident beam polarized parallel to x, y, and z. (d) A cut along the L direction for all three cross sections. The cuts were integrated over the range $0.9 < H < 1.1$.

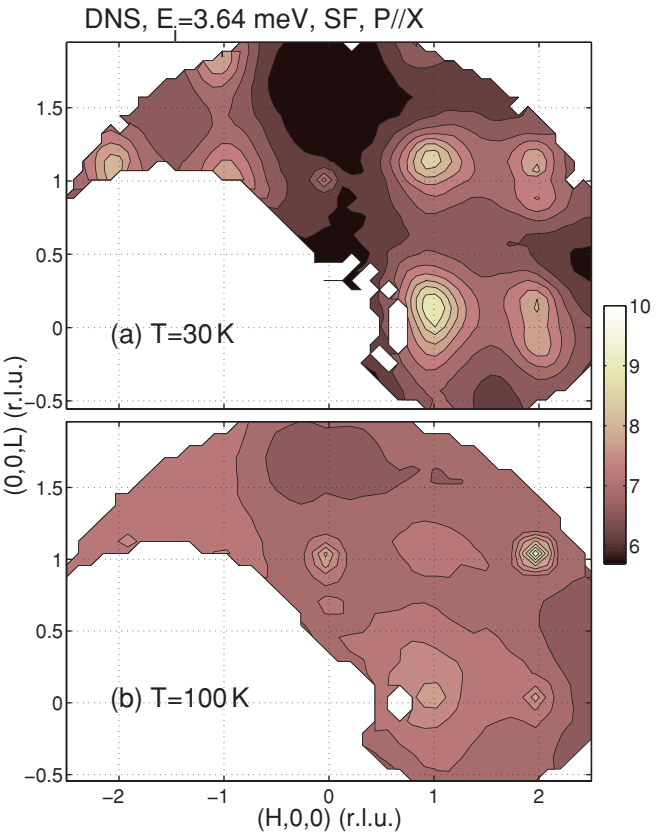

FIG. 4. (Color online) Spin-flip cross section with incident polarization parallel to x is illustrated at (a) 30 K and (b) 100 K. Data are plotted on a log scale. Data on DNS were taken with $E_i = 3.64$ meV.

indicates that the scattering is isotropic to a first approximation, as expected for paramagnetic scattering above T_N. There is a difference between the spin-flip cross sections in the y and z channels, with the z cross section being larger than the y channel at $\vec{Q} = (1,0,0)$. This indicates a small anisotropy between the paramagnetic scattering above T_N and may be expected given the highly anisotropic structure reported.[21]

Figure 4 illustrates the temperature dependence of the contours of magnetic scattering above T_N at 30 K [Fig. 4(a)] and 100 K [Fig. 4(b)]. Both data sets were taken with the incident beam polarization parallel to x and therefore are a measure of the total magnetic scattering cross section. The data are plotted on a logarithmic scale. Since x is parallel to the average $\vec{Q}$ and no analyzer crystal was used, these scans provide an approximate measure of the total energy-integrated magnetic scattering cross section. At $T = 30$ K, well-defined diffuse scattering contours exist around the incommensurate positions at $q_0 = (0,0,\sim 0.15)$, where magnetic ordering was observed below T_N. At $T = 100$ K, clear diffuse scattering is present, although much reduced in intensity and considerably broader in momentum, indicating a decrease in the correlation length. It is interesting to note that the contours of constant scattering intensity imply an anisotropic line shape that is broader in the [100] direction than the [001]. This implies that the c-axis correlations are significantly stronger and therefore it is important to determine the c-axis magnetic exchanges

in understanding the critical and physical properties of this system. We return to this point later when discussing the spin waves at low temperatures.

As pointed out in Ref. 34, a vector chirality variable can be defined by Eq. (2) and is proportional to the cross product in the second term in Eq. (1). This chirality should occur simultaneously with spin ordering and follow a power-law divergence similar to the magnetic order parameters in conventional second-order phase transitions. This order parameter can be derived in polarized neutron scattering experiments as the difference between the two spin-flip cross sections I^{+-} equal to I^{-+} when the neutron polarization is parallel to the momentum transfer vector. Therefore, near the phase transition the difference between the two spin-flip channels and the value of the incommensurability should go to 0. We have investigated this quantity using the DNS polarized neutron diffractometer.

The difference between the spin-flip cross sections I^{+-} and I^{-+} with the incident neutron polarization parallel to the x axis is displayed in Fig. 5. Figures 5(a)–5(c) plot the subtracted intensity $I^{+-} - I^{-+}$, which is sensitive to the chirality parameter discussed above. If there were no chirality present, then the cross product in the Eq. (1) would vanish and the difference would be 0. All panels at temperatures ranging from 30 to 100 K clearly show the presence of correlated magnetic scattering with a vector chiral component, even at 100 K, well above the ordering temperature of 27 K. The magnetic scattering is also clearly displaced away from the nuclear Bragg peak positions and located close to the position in momentum where the magnetic Bragg peak is observed at low temperatures. As these measurements integrate in energy, we are not able to determine from these scans if this diffuse scattering is dynamic or static or on what time scale the fluctuations occur. This is discussed in the next section with energy-resolved triple-axis and direct geometry chopper measurements. The white gaps near the nuclear Bragg peak positions in Fig. 5 are regions where the strong feed-through from the non-spin-flip channel as a result of nuclear scattering did not subtract well and hence has been removed from the data for clarity.

To confirm the experimental setup, we plot a similar analysis, but with the incident polarization parallel to the z axis, in Fig. 6. This is an important check, as the difference observed above could result from differences in the flipping ratios between the $+x$ and the $-x$ configurations. One of the two cross sections (I^{+-}) is illustrated in Fig. 6(a), with Fig. 6(b) plotting a cut of both I^{+-} and I^{-+}. Figure 6(c)

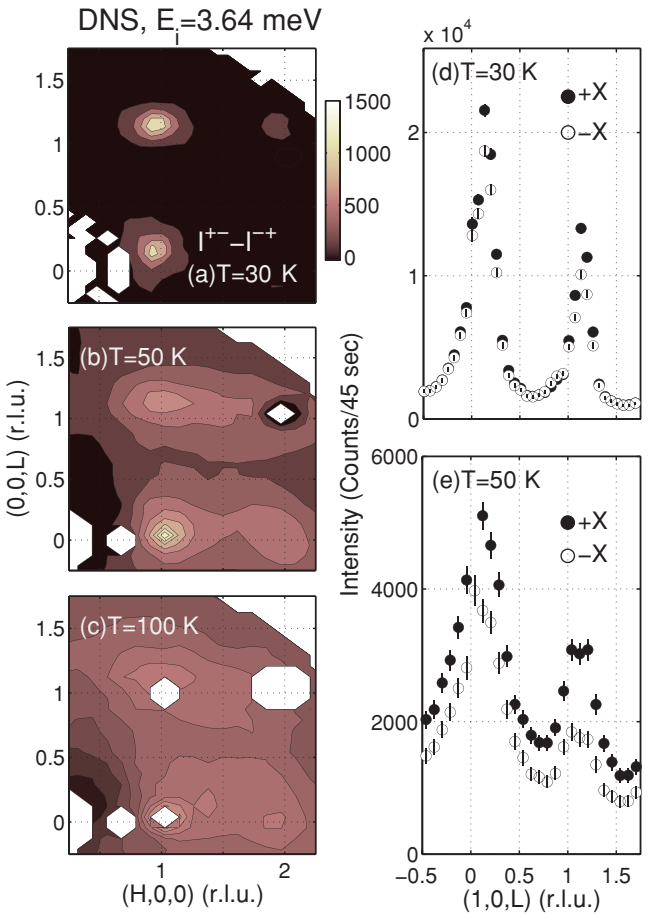

FIG. 5. (Color online) Spin-flip cross section with incident polarization parallel to x and $-x$. (a–c) The difference between the spin flip cross sections I^{+-} and I^{-+} at several temperatures. (d, e) Linear cuts along (1,0,L) illustrating the difference between the two cross sections. Cuts were integrated over the range $0.9 < H < 1.1$.

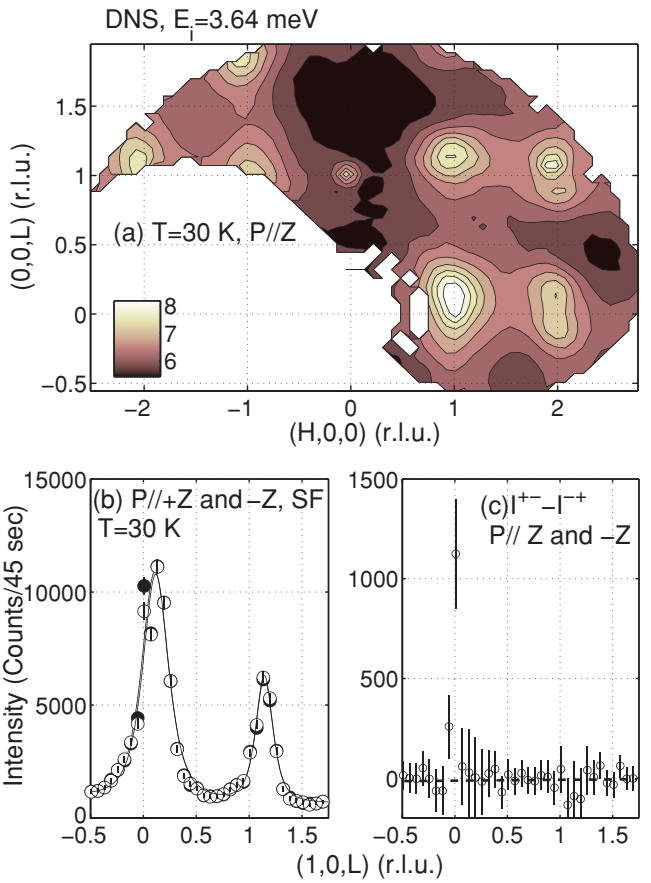

FIG. 6. (Color online) Spin-flip cross section with incident polarization parallel to z and $-z$. (a) Contours of the raw intensity with the beam parallel to z and hence showing I^{+-}. (b) Comparison between I^{+-} and $I-+$. Cuts were integrated over the range $0.9 < H < 1.1$. (c) A subtraction of the two cross sections, illustrating no difference within experimental error.

confirms that there is no difference between the two cross sections to within experimental error except near the Bragg position ($L = 0$), where the feed-through from the non-spin-flip cross section contaminates the data and does not subtract out fully. This complete subtraction is the result expected for the spin-flip cross section when the incident beam polarization is perpendicular to the momentum transfer. This confirms the quality of the experiment, the results, and the conclusions applied to the data taken with the polarization parallel to x described above.

The results here are quite surprising given that the chirality (as defined in Ref. 34) is predicted to diverge at T_N, yet we still observe a strong chirality at temperatures more than three times T_N. This is in contrast to the results reported in MnSi, which is a prototypical spiral magnetic resulting from the Dzyaloshinski-Moriya interaction. While polarized work near the transition temperature has measured a finite difference between the two spin-flip cross sections, indicating chiral fluctuations,[42] at much higher temperatures the difference between the two cross sections has been found to become significantly smaller.[33] This is also the case in holmium, where the difference falls to 0 above the transition temperature.[28] Indeed a Landau free-energy expansion did show that the two cross sections (I^{+-} and I^{-+}) should become equal at high temperatures, consistent with the high-temperature experimental data. This is clearly not the case in $Ba_3NbFe_3Si_2O_{14}$ and implies that a physical picture utilizing a dominant Dzyaloshinski-Moriya interaction must be examined carefully. In the next section we discuss the energy-resolved critical dynamics measured with both a chopper instrument and a cold triple-axis.

C. Spin fluctuations and critical properties

To understand the critical properties, we investigated the critical spin fluctuations near the ordering temperature using both powder and single-crystal samples. The inelastic spectrum at several temperatures in the powder is summarized in Fig. 7, with the data taken on MARI using $E_i = 10$ meV. The low-temperature ($T = 4$ K) spectrum is discussed in detail later but the higher temperatures illustrate the presence of strong magnetic fluctuations above the ordering temperature of $T_N = 27$ K. To extract a line width as a function of temperature, we have fit a series of constant-Q cuts to the formula

$$S(E) = \chi_0[n(E) + 1]\frac{E\Gamma}{\Gamma^2 + E^2}, \tag{3}$$

where χ_0 is the real part of the susceptibility, Γ is the energy half-width, and $n(E) + 1$ is the Bose factor. This formula allows us, from a constant-Q scan, to extract the real part of the susceptibility (χ_0) and an energy line width (Γ). Examples of the resolution convolved fits extracted from the MARI data above T_N are shown in Fig. 8.

Constant-Q cuts taken using the PANDA cold triple-axis spectrometer on single-crystal samples are presented in Fig. 9. These scans were performed at the measured ordering wave vector and the solid lines are fits to Eq. (3) plus a δ function centered at the $E = 0$ elastic position defined by the energy resolution. Similarly, from these scans we are able to extract parameters for the susceptibility χ_0 and the energy line width Γ.

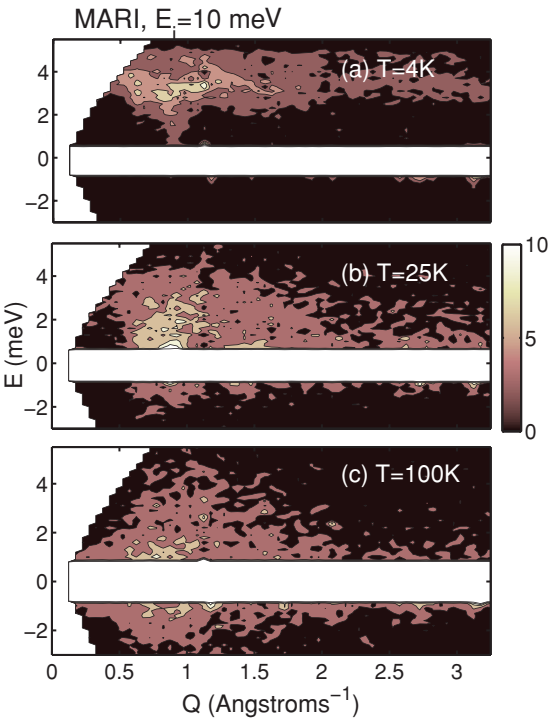

FIG. 7. (Color online) A series of contour plots of the magnetic scattering in $Ba_3NbFe_3Si_2O_{14}$ at a series of temperatures. Data were taken on the MARI direct geometry chopper spectrometer located at ISIS, with a fixed incident energy $E_i = 10$ meV and at a Fermi chopper speed of 250 Hz.

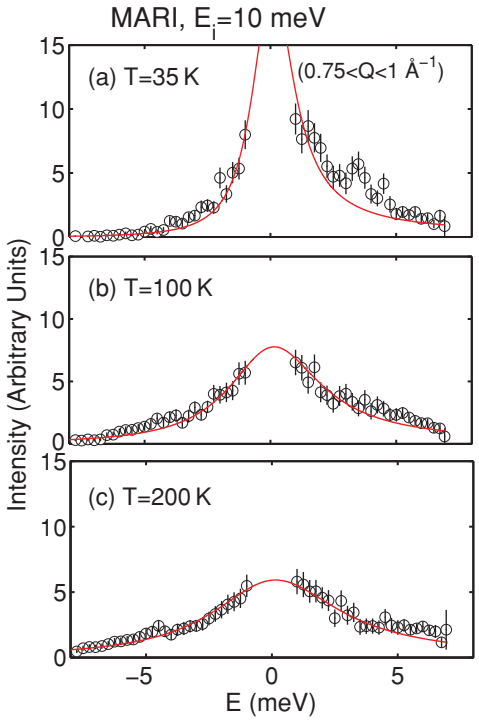

FIG. 8. (Color online) A series of constant-Q cuts taken from the $E_i = 10$ meV MARI data above T_N. Solid curves are fits to the modified Lorentzian discussed in the text. Data illustrate strong critical fluctuations that broaden with increasing temperature.

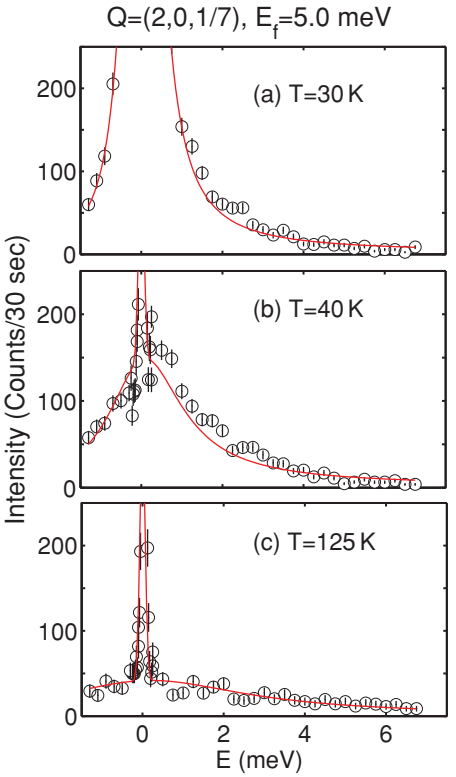

FIG. 9. (Color online) A series of constant-Q scans taken on the PANDA cold triple-axis using a fixed final energy of $E_f = 5.0$ meV at $\vec{Q} = (1,0,1/7)$. Solid curves are fits to the modified Lorentzian discussed in the text plus the resolution function centered at the elastic energy ($E = 0$ meV).

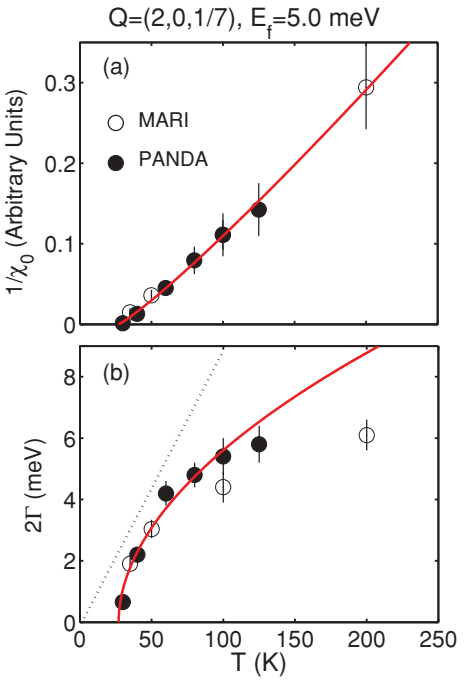

FIG. 10. (Color online) (a) Plot of the inverse of the real part of the susceptibility $1/\chi_0$ as a function of temperature for data taken on both powder (MARI) and single-crystal (PANDA) samples. (b) The full width (2Γ) is plotted against temperature. The dashed line is $2\Gamma = k_B T$. Solid curves are the power laws described in the text and previously measured in two-dimensional triangular antiferromagnets.

A summary of the temperature dependence of χ_0 and Γ is illustrated in Fig. 10. The scaling factor for the susceptibility between the MARI and the PANDA data were obtained from a common temperature taken at 100 K. The two data sets overlap very well, illustrating a consistent analysis. A plot of χ_0^{-1} [Fig. 10(a)] illustrates a smooth function that intercepts the x axis at the Neel temperature, indicating that the transition is likely second order. The solid curve is a plot of $\chi_0 \propto (T - T_N)^{-\gamma}$, with $\gamma = 1.1$. This is the same critical exponent predicted and measured for the strongly two-dimensional triangular magnets $CsMnBr_3$, and $CsVCl_3$.[34–36]

A plot of the line width 2Γ as a function of temperature above T_N is illustrated in Fig. 10(b). The solid line is a plot of the power law $\Gamma \propto (T - T_N)^{\nu}$, with $\nu = 0.53$, as found for the two-dimensional triangular systems described above. The line width (Γ) can be related to the correlation length using hydrodynamic theory, which states that $\Gamma \propto \hbar c/\xi$, where $\hbar c$ is the spin-wave velocity and ξ is the correlation length.[39] Given that the correlation length scales as $\xi \propto (T - T_N)^{-\nu}$, we have used the same power-law form to describe the line width in Fig. 10(b).

The dashed line in Fig. 10(b) is a plot of $2\Gamma = k_B T$ and illustrates that the line width we observe is always less than the energy scale set by the temperature ($k_B T$). This indicates that the dynamics and critical fluctuations are in the classical limit, in contrast to frustrated magnets with a lower spin value, for example, $NiGa_2S_4$ or in the superconductor YBa_2CuO_{6+x}, where $2\Gamma > k_B T$.[7,40,41] These results indicate that the critical scattering in $Ba_3NbFe_3Si_2O_{14}$ is indeed classical in nature. The steep increase in the line width just above the Neel temperature indicates that the diffuse magnetic scattering discussed in the previous section (which integrates in energy up to ~3 meV) is primarily dynamic, and therefore the critical fluctuations above T_N retain a chiral character, resulting in the difference between the positive and the negative spin-flip channels.

In summary, we have combined chopper and triple-axis measurements on single crystals and powders to obtain the temperature dependence of the energy line width (2Γ) and the susceptibility (χ_0). The temperature dependence is consistent with the power laws derived in other two-dimensional triangular magnets where $\gamma = 1.1$, $\beta = 0.25$, and $\nu = 0.53$ and indicates that the transition is second order and that the fluctuations near T_N behave classically.[34]

IV. SPIN-DIMER CALCULATION

The paramagnetic properties outlined in the previous section are very different from those measured in simple helical magnets where the structure is driven by a dominant Dzyaloshinkskii-Moriya interaction. While the critical fluctuations behave in a consistent manner to other triangular magnets adopting a 120° structure, the presence of a chiral signal with polarized neutrons up to temperatures of at least 100 K is somewhat surprising. We now investigate the symmetric exchange constants and begin this analysis by estimating the various exchange interactions using a spin-dimer formulation. The crystal structure for the left-handed chirality is represented in Fig. 1, projected in the ab plane [Fig. 1(a)] and along

TABLE I. Bonding (ϵ_{ii}) and antibonding ($\epsilon_{ii}*$) energy levels for the five molecular orbital levels illustrated in Fig. 11.

SSE interaction	J_1	J_2	J_3	J_4	J_5
d(Fe-Fe) Å	3.692	5.652	6.411	5.241	6.411
d(O-O) Å	2.769	2.624	3.965	2.901	2.774
ϵ_{11} (eV)	–12.329	–12.260	–11.878	–11.793	–11.514
$\epsilon_{11}*$ (eV)	–12.323	–12.248	–11.856	–11.732	–11.464
ϵ_{22} (eV)	–12.333	–12.258	–11.869	–11.794	–11.518
$\epsilon_{22}*$ (eV)	–12.316	–12.251	–11.861	–11.741	–11.485
ϵ_{33} (eV)	–12.327	–12.257	–11.867	–11.773	–11.510
$\epsilon_{33}*$ (eV)	–12.326	–12.255	–11.866	–11.772	–11.508
ϵ_{44} (eV)	–12.329	–12.267	–11.870	–11.776	–11.510
$\epsilon_{44}*$ (eV)	–12.323	–12.238	–11.862	–11.768	–11.508
ϵ_{55} (eV)	–12.327	–12.257	–11.885	–11.774	–11.522
$\epsilon_{55}*$ (eV)	–12.326	–12.254	–11.840	–11.772	–11.483
$\langle(\Delta\epsilon)^2\rangle$ (meV^2)	6868	4282	9	1009	3627

the c axis [Fig. 1(b)]. Exchange paths are indicated by the label J_i ($i = 1,5$) following the conventions used in Ref. 21. All exchange terms are dominated by contributions from super superexchange (SSE) through Fe^{3+}-O-O-Fe^{3+} since there are no covalent Fe^{3+}-O-Fe^{3+} bonds. J_1 and J_2 are, respectively, the nearest-neighbor and next-nearest-neighbor exchange interactions in the ab plane. Along c, there are three inequivalent exchanges paths connecting adjacent layers. J_4 connects each of the Fe^{3+} ions in a triangular unit to ions directly above, that is, related by the lattice translation (0,0,1). J_3 and J_5 link different Fe^{3+} ions of adjacent triangles and create *helical* paths along the c axis of opposite chirality (anticlockwise for J_3 bonds and clockwise for J_5 bonds). The relative strengths of the different SSE terms are determined by the overlap of the O p-wave functions, which depend greatly on the value of the O-O distance with respect to the van der Waals distance (2.80 Å) and the value of the Fe^{3+}-O-O-Fe^{3+} dihedral angle. Relevant bond distances are presented in the top row in Table II.

The relative strengths of the five SSE interactions have been derived semiquantitatively by a spin-dimer analysis based on extended Huckel tight-binding (EHTB) calculations.[37] The atomic orbitals for Fe and O are approximated by double-ζ Slater orbitals, using the parameters listed in the supplementary information to Ref. 38. The Fe^{3+} ion is in a distorted tetrahedral configuration (point symmetry 2), and the nonbonding E_g levels and antibonding T_{2g} levels found for Td symmetry splits into singlets $E_g \rightarrow 2A$ and $T_{2g} \rightarrow A \oplus 2B$. The molecular orbitals of the FeO_4^{5-} complex calculated by EHTB are shown in Fig. 11 (and see Table I). Each singlet (labeled $\mu = 1,5$ from the lowest to the highest energy) is occupied by a single electron due to the high-spin d^5 electronic configuration of Fe^{3+}. The antiferromagnetic contribution of each of the SSE interactions can be evaluated in turn by considering the corresponding $Fe_2O_8^{10-}$ dimer and calculating the average of the squared energy difference between the bonding (ϵ_{ii}) and the antibonding ($\epsilon_{ii}*$) states for each energy level:

$$J \propto \langle(\Delta\epsilon)^2\rangle \propto \sum_{\mu=1,5} (\Delta\epsilon_{\mu\mu})^2, \tag{4}$$

where the sum runs over the five sets of bonding-antibonding states resulting from correlations between pairs of all the 3A and 2B molecular orbitals. Essentially the values of $\langle(\Delta\epsilon)^2\rangle$ are proportional to the square of the hopping integral (t^2), that is, to the exchange energies. The results are listed in Table II. The strongest exchange interaction is J_1, slightly stronger that the other in-plane exchange J_2. Along the c axis, J_5 is by far the strongest exchange, as already pointed out in Ref. 21, and approximatively four times larger than J_4. Due to the very long O-O distance, J_3 is negligible in comparison with all other exchange terms.

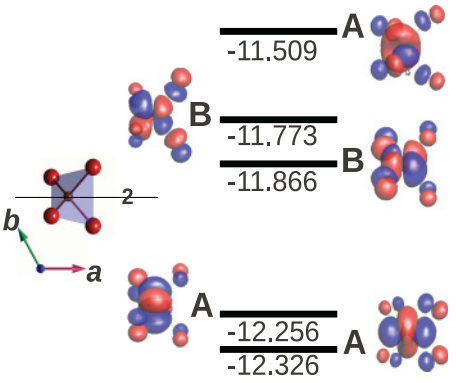

FIG. 11. (Color online) Molecular orbitals of the FeO_4^{5-} complex calculated by the extended Huckel tight-binding method (see text for details). The five levels (all singlets) are shown with their corresponding energy (in eV), their symmetry label, and a drawing of the molecular orbitals. At the left, a FeO_4 tetrahedra is shown in the same projection along the c axis. The unit-cell axes and position of the twofold symmetry axis are also shown.

Applying Eq. (4) and normalizing to the value J_4, we summarize the following for the relative values of J_{1-5}:

$$J_1/J_4 = 6.8, \quad J_2/J_4 = 4.2, \quad J_3/J_4 \sim 0, \\ J_4/J_4 = 1, \quad J_5/J_4 = 3.6. \tag{5}$$

We now investigate the low-temperature spin waves that are characterized by the exchange constants and use these values to motivate a spin-wave model to describe the dispersion curves.

V. LOW-TEMPERATURE SPIN WAVES

In this section we discuss the spin waves measured in the Neel-ordered state at low temperatures. We first present the data measured both along (00L) and along (H00) directions. We then present a heuristic model for the spin interactions that map onto an XY Hamiltonian consistent with our analysis of the critical fluctuations, which is strongly suggestive of a such a character for the spins. This model provides a means of estimating the exchange constants along [00L] ($J_{i=3-5}$). We then derive estimates for the exchange constants within the a-b plane ($J_{i=1,2}$). Using the values for the exchange constants derived from the spinwaves, we derive expressions for the ordering wave vector and the Curie-Weiss constant and compare with experiment. We focus our discussion on the spin dynamics along the c^* direction, as these have the most relevance for the incommensurability.

A. Experimental data

In this section we present measurements of the spin waves that characterize the low-temperature magnetic ground state. To obtain an overview of the magnetic scattering we first conducted preliminary measurements on MARI. The low-temperature spectrum is illustrated in Fig. 7(a), which illustrates a total spin band width of about 4–5 meV and a mode extending to the lowest energies at $Q \sim 0.85$ Å^{-1}. This wave vector is consistent with magnetic wave vector value of $\vec{Q}_0 = (1,0,\sim 1/7)$ derived from the magnetic structure.

To investigate the spin waves further, we performed measurements on a single crystal using the PANDA cold triple-axis spectrometer. Given the spiral pitch along the (00L) direction, we focused our measurements on the spin-wave dispersion along c^* in an effort to determine the origin of the incommensurate wave vector. The results are illustrated in Fig. 12 where Fig. 12(a) illustrates a contour plot of the measured intensity and Figs. 12(b)–12(d) are representative constant-Q scans. While the spectrum is quite complex, it can be understood in terms of three branches. There is one branch that originates from the incommensurate Bragg peak [$\vec{Q} = (2,0,1/7)$] and rises up to ∼2 meV at the nuclear zone center [$\vec{Q} = (200)$]. At $\vec{Q} = (200)$ we observe two gapped modes. One disperses up to ∼4.5 meV at the zone boundary [$\vec{Q} = (2,0,0.5)$] and the other one disperses only up to ∼3 meV. The solid curves in Figs. 12(b)–12(d) are fits to Lorentzians without resolution convolution to extract the energy position.

We investigated the low-energy spin waves near the incommensurate-ordering wave vector of $\vec{Q} = (2,0,1/7)$ by

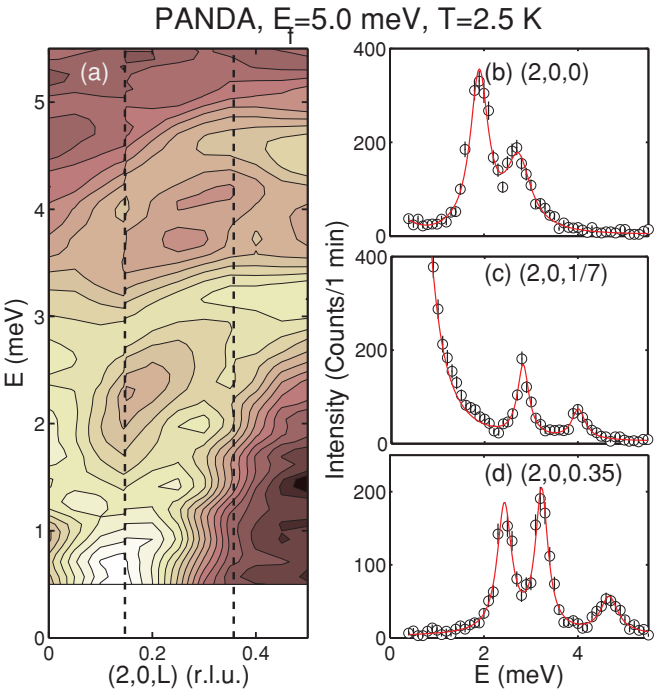

FIG. 12. (Color online) (a) Contour plot of spin waves measured along the (00L) direction. Data are plotted on a logarithmic scale. (b–d) Representative constant-Q cuts at a serious of wave vectors throughout the Brillouin zone.

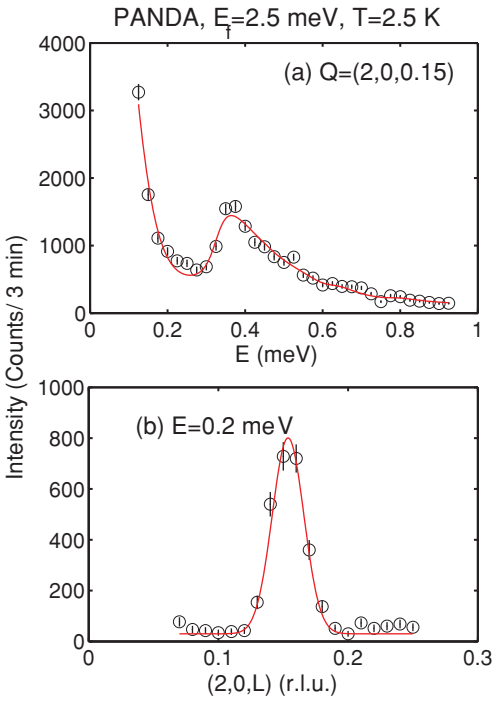

FIG. 13. (Color online) (a) Constant-Q scan at $\vec{Q} = (2,0,0.15)$; $T = 2.5$ K and $E_f = 2.5$ meV. A gapped mode is clearly present at 0.35 meV. (b) Constant-energy scan performed below the gapped mode illustrating the presence of magnetic scattering below the gapped mode and the presence of a gapless phason mode.

using a fixed final energy of $E_f = 2.5$ meV. As outlined in Sec. II, this provided increased energy resolution. A summary of the results is displayed in Fig. 13, with Fig. 13(a) illustrating a constant-Q scan performed at the ordering wave vector. A constant-energy scan at low-energy transfers of $E = 0.2$ meV is shown in Fig. 13(b). The solid curves are resolution-convolved fits to a gapped mode and a gapless excitation originating from the incommensurate Bragg peak. The inclusion of resolution in the fits is necessary to achieve the high-energy tail of the peak in Fig. 13(a). The results illustrate the existence of two modes originating from the ordering wave vector at $\vec{Q} = (2,0,1/7)$: one gapless and one gapped with a value of 0.35 meV. These modes become degenerate above the gap value within experimental resolution. The dispersion curves along the (00L) direction are sensitive to the exchange constants along the c direction illustrated in Fig. 1 and labeled $J_{3,4,5}$. A model used to derive these parameters and interpret the physical nature of these modes is presented in the next section.

Having shown the experimental results for the spin waves along (00L) direction, we now show the results along the (H00) direction. A summary of a series of constant-Q scans taken along the (H,0,6/7) direction is displayed in Fig. 14, with a false contour plot in Fig. 14(a) and constant-Q scans in Figs. 14(b)–14(d). The scans illustrate that the three modes observed at the incommensurate-order wave vector disperse and become more well separated along the (H,0,6/7) direction. The dispersion of these modes is sensitive to the in-plane exchange constants, namely, the exchange within a given triangle (J_1) and the exchange between triangles (J_2). Values

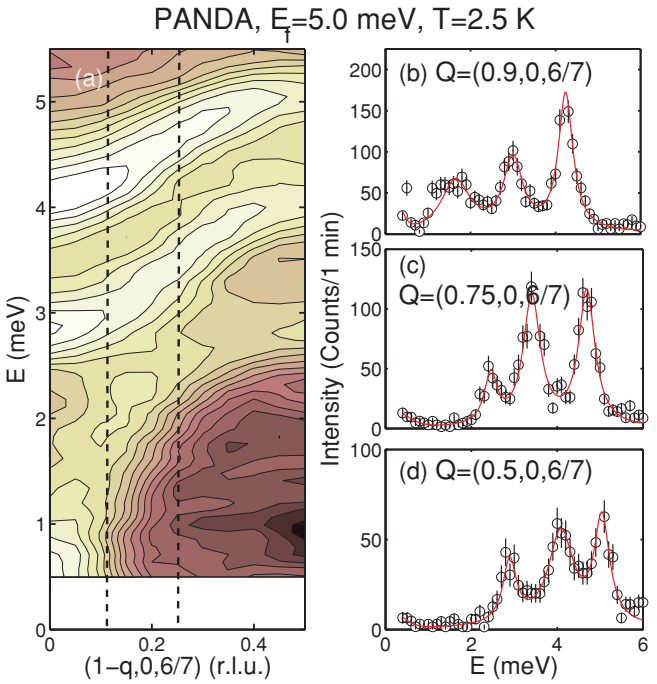

FIG. 14. (Color online) (a) A false contour plot summarizing the constant-Q scans along the $(1-q,0,6/7)$ direction taken on PANDA with $E_f = 5.0$ meV. (b–d) Representative constant-Q scans.

of these exchange constants are estimated and are presented in the next section.

B. Spin waves along the (00L)

Most spiral magnets have the chirality imposed by the Dzyaloshinski-Moriya interaction (characterized by the vector $\vec{D}$), which appears in the Hamiltonian as a cross product of spins ($\vec{D} \cdot \vec{S}_1 \times \vec{S}_2$). While such a model may fit the low-energy spin waves described above, we find that to consistently describe the observed spin-wave band width (defined by J) and the incommensurate wave vector [described by the spiral pitch $\alpha = \arctan(D/J)$] would require $D \sim J$. This is unphysical given that D is a relativistic correction related to spin-orbit coupling and hence expected to be small in comparison to the spin-exchange J for a d^5 high-spin electronic state with quenched total orbital momentum ($L = 0$). Only a very low orbital momentum would be expected due to the slightly distorted tetrahedral configuration of $Fe^{3+}O_4$, with a slight off-centering of Fe.

We have taken a different approach to this problem motivated by the structure (Fig. 1), the spin-dimer calculations, and the polarized neutron scattering results presented earlier. We now investigate whether the physical properties, including the incommensurate order wave vector, the spin waves, the Curie-Weiss constant (Θ_{CW}), and, most importantly, the magnetic chirality, can be understood in terms of a Heisenberg only framework. The Fe^{3+}-O^{2-} coordination is plotted in Fig. 1 and illustrates that all of the exchange paths are super-superexchange involving two oxygen ions. The structure along the c axis [Fig. 1(b)] illustrates that the two next-nearest-neighbor interactions (J_3 and J_5) have very different exchange

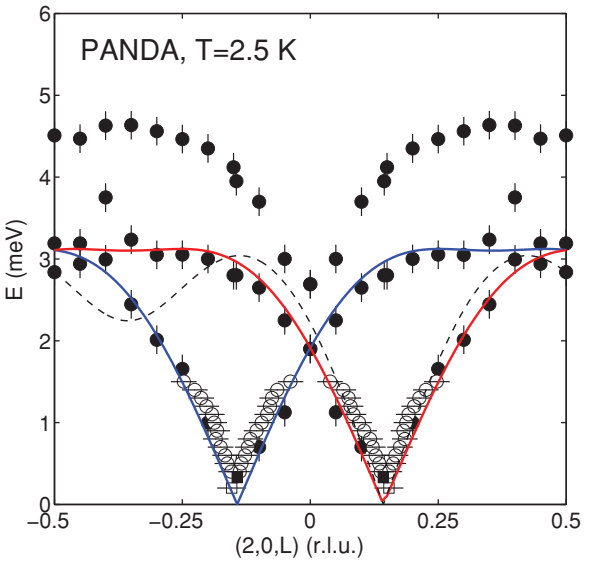

FIG. 15. (Color online) Plot of the peak position in energy as a function of momentum transfer along the c^* direction ($00L$). Solid lines are fits to the spin-wave models discussed in the text. The dashed line is a calculation with J_3 fixed to 0 and just fitting J_4 and J_5. Data have been symmetrized around $L = 0$ for clarity.

paths imposed by the crystal symmetry. We now discuss a model for the spin waves along the c direction.

Based on this analysis, we can then use the formulas presented in Ref. 46 to obtain the spin-wave dispersion along (00L). We write a mean field description of the spin waves in the Appendix which predicts the existence of three gapless modes emanating from the incommensurate positions ($L = \pm\alpha$) and the commensurate position ($L = 0$).[6,48] The data presented in the previous section does display gaps in the excitations spectrum and these maybe understood in terms of a single-ion anisotropy as done in $TbMnO_3$.[47,48]

Figure 15 illustrates extracted peak positions, based on constant-Q scans (filled circles) and constant energy scans (open circles), obtained using the Panda cold triple-axis spectrometer. The data clearly show the presence of two gapless modes originating from the incommensurate points ($L = \pm\alpha$) with a bandwith of ~3 meV. At least one more mode is measured which extends to higher energies and may originate from the commensurate $L = 0$ position.

The model presented in the Appendix provides a physical understanding of the spin waves and a fit to the lowest energy gapless mode is illustrated in Fig. 15 by the solid lines. These modes represent the phason required for a spiral structure and corresponds to a rigid rotation of the spins within the spiral plane. While our mean field analysis captures the presence of gapless modes at the two incommensurate position ($L = \pm\alpha$), it fails to describe the higher energy scattering particularly near the commensurate ($L = 0$) position. As suggested by J. Jensen, a mean field analysis based on a simple helix would predict a single peak in a constant momentum scan at $\vec{Q} = (2,0,0)$ position where our data (Fig. 12(b)) clearly shows two peaks present at this commensurate position.[44,49] As discussed in the Appendix, we believe that a full description of all of the spin-wave branches may require more complex calculations and therefore we fit only the lowest energy gapless modes

TABLE II. A summary of exchange constants measured and also predicted by the spin-dimer analysis described in the text.

i	$J_{i,\mathrm{exp}}$	$J_{i,\mathrm{exp}}/J_{4,\mathrm{exp}}$	$J_{i,\mathrm{calc}}/J_{4,\mathrm{calc}}$
1	1.6 ± 0.3 meV	16 ± 3	6.8
2	0.31 ± 0.05 meV	3.1 ± 0.6	4.2
3	0.13 ± 0.02 meV	1.3 ± 0.2	~ 0
4	0.10 ± 0.02 meV	1	1
5	0.33 ± 0.02 meV	3.3 ± 0.5	3.6

which emanate from $L = \pm\alpha$ to obtain a set of exchange constants.

A fit to the lowest energy gapless modes originating from the incommensurate positions (as illustrated by the solid lines) yields the following parameters,

$$\begin{aligned} J_3 &= 0.13 \pm 0.02 \text{ meV} \\ J_4 &= 0.10 \pm 0.02 \text{ meV} \\ J_5 &= 0.33 \pm 0.02 \text{ meV} \end{aligned} \tag{6}$$

While the low-energy gaps near the incommensurate positions may result from single-ion anisotropies, we do not attempt to model them owing to the fact that the gaps are small in comparison to the total bandwidth of the excitations.[49]

These parameters are broadly consistent with the spin-dimer calculations that predict a helical set of exchange constants and a direct comparison, including the values of J_1 and J_2 derived below, are summarized in Table II. The magnitudes are generally consistent with the calculation except the value of J_3 is much larger than predicted but is required to provide a good fit to the spin-wave dispersion near the Brillouin zone boundary. The spin-wave formulation for the excitations along $(00L)$ are quite sensitive to the values of J_3, particularly near the zone boundary. This is demonstrated in Fig. 15 by the dashed line, which is a calculation with J_3 fixed to be 0 and $J_5 = 0.5$ meV. To obtain the relatively flat dispersion of the modes near the zone boundary, a relatively large value of J_3 is required within our formulation. The spin-wave calculation is equally sensitive to J_4. While we can reproduce the flat nature near the zone boundary and the bandwidth with competing J_4 and J_5 values only, such a model does not fit the initial slope of the modes near the magnetic Bragg peaks. This spin-wave model therefore provides a sensitive determination of $J_{3,4,5}$. As a check of our analysis, we now use the derived values of $J_{3,4,5}$ to calculate the ordering wave vector and compare the value with experiment.

C. Incommensurate-ordering wave vector q_0

The ordering wave vector defined by the pitch α can be obtained by calculating the classical minimum of the Hamiltonian defined above. The classic exchange energy for the spiral magnetic structure proposed by Marty *et al.*,[21] independent of any Dzyaloshinskii-Moriya interaction, can be written

$$\begin{aligned} E(\alpha) &= \sum_i J_4 \vec{S}_i^a \cdot \vec{S}_{i+1}^a + J_3 \vec{S}_i^a \cdot \vec{S}_{i+1}^b + J_5 \vec{S}_i^a \cdot \vec{S}_{i+1}^c \\ &= N[J_4 \cos(\alpha) + J_5 \cos(\alpha + 2\pi/3) \\ &\quad + J_3 \cos(\alpha - 2\pi/3)], \end{aligned} \tag{7}$$

where N is the number of cells considered along the c axis, and the sum (i) runs from 1 to N. This is the energy for the left-handed crystal structure and the negative triangular chirality. We have assumed that the Umklapp terms sum to 0 as expected for an incommensurate structure. The energy for the positive triangular chirality can be obtained by changing $2\pi/3$ into $-2\pi/3$, and vice versa. The in-plane exchange energy is irrelevant here because it does not depend on α. The magnetic modulation is considered incommensurate ($\tau \sim \frac{1}{7}$); that is, the summation runs over an infinite number of sites, and only normal terms contribute to the energy (Umklapp terms sum up to 0 for an incommensurate structure). The resulting functional of the energy is extremely interesting, because it is not invariant by a change of sign of α. Changing α to $-\alpha$ is equivalent to permuting J_3 and J_5, and our previous analysis showed that these two exchange interaction have very different strengths. This demonstrates that for a given triangular chirality, a single magnetic chirality is stabilized by isotropic exchanges alone, whose strengths are imposed by the chiral crystal structure. The stability condition for the energy ($dE/d\alpha = 0$) leads to the following incommensurability [defined by $\tan(\alpha)$] in terms of the three exchange parameters ($J_{3,4,5}$) defined above:

$$\tan(\alpha) = \frac{\sqrt{3}(J_3 - J_5)}{2J_4 - (J_5 + J_3)}. \tag{8}$$

Substituting the values extracted from the spin-wave dispersion along c^* for $J_{3,4,5}$, we find

$$q_0 = \frac{\alpha}{2\pi} = 0.148 \pm 0.007 \text{ r.l.u.}, \tag{9}$$

in very good agreement with the experimental value of 0.143 r.l.u. For the opposite triangular chirality, the value of q_0 will be reversed. Both structures are compatible with the results of Marty *et al.* derived from neutron polarimetry.[21] This illustrates a consistent description of the incommensurate wave vector and the spin waves in terms of a Heisenberg only model for the spin interactions. This result also corroborates the spin-wave analysis, which implies that all three competing exchange constants are required to describe the dynamics. We note that a J_4-J_3 or a J_4-J_5 only picture cannot describe the incommensurate wave vector. We emphasize also that while the Dzyaloshinskii-Moriya interaction is present owing to the low crystal symmetry, our analysis shows that it is not required and would only be a small perturbation to the energy *asymmetry* between J_3 and J_5, which determines the ordering wave vector. In fact, one can rewrite Eq. (7) to include three different Dzyaloshinskii-Moriya interactions alongside the three exchange paths. We consider only the z component of the DM vectors, which couples to the in-plane spin structure, labeled by DM_i ($i = 3,4,5$). The stability condition becomes

$$\tan(\alpha) = \frac{\sqrt{3}(J_3 - J_5) + 2\mathrm{DM}_4 + \mathrm{DM}_3 - \mathrm{DM}_5}{2J_4 - (J_5 + J_3) + \sqrt{3}(\mathrm{DM}_5 - \mathrm{DM}_3)}. \tag{10}$$

It is clear that for Fe^{3+}, the strengths of the DM terms (proportional to $\frac{\Delta g}{g} J$) will be at best only a few percent of the isotropic terms and will not play any role in selecting a given magnetic chirality, unless for accidental degeneracies of the different J terms. The values extracted from the spin-wave analysis indicate that this is not the case here.

Since the single magnetic chirality (sign of α) depends on the initial choice of the triangular chirality, the question remains about the absolute chirality of the system. However, it is important to realize that the magnetic structures corresponding to the positive and negative triangular chiralities are supported by different irreducible representations of the $P321$ group (totally symmetric τ_1 for positive triangular chirality and τ_2 for negative). The presence of single-ion anisotropy or in-plane Dzyalonshinskii-Moriya terms, which are present (however small) due to the twofold symmetry on the Fe^{3+} site, will actually select a unique triangular chirality; a unique magnetic state will be stabilized.

D. Spin waves within the *a-b* plane

To extract information on the exchange parameters within the *a-b* plane, we investigated the spin-wave dispersion along the (H,0,6/7) and (H,0,0) directions and along the zone boundary (H,0,0.5). The spin-wave dispersion along (H,0,6/7) is presented in Fig. 16(a). While our analysis above for spin waves along the (0,0,L) direction does not provide direct information on the exchange within a triangle J_1, the initial slope of the lowest energy mode along the (H,0,1/7) can be interpreted as a first approximation for this

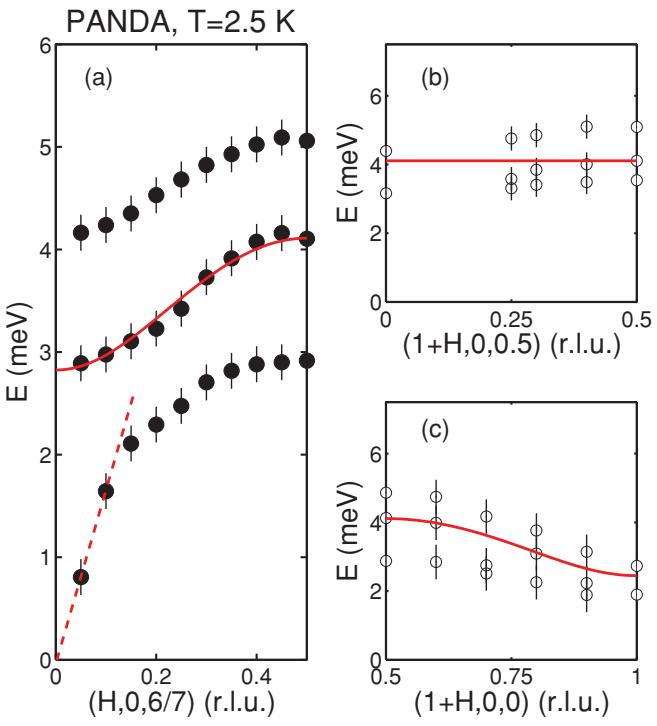

FIG. 16. (Color online) Dispersion curves within the *ab* plane extracted from the analysis described in the text. (a) Peak positions along the (H,0,6/7) direction. The dashed line is used to estimate the exchange within a triangle (J_1). Solid lines are derived from the general expression described in the text for antiferromagnetic exchange. (b) Peak positions around the zone boundary, illustrating relatively little dispersion, which indicates small next-nearest-neighbor exchange. (c) Dispersion along the ($1+H$,0,0) direction. The solid curve is a calculation by the same formula used in (a), but with a finite value of Δ to account for not being exactly at the magnetic-zone center.

exchange parameter. Using the second moment sum rule,[50] which relates $S(\vec{Q},E)$ to the dispersion $E(\vec{Q})$ as $\langle E(\vec{Q})^2\rangle = \int dE E^2 S(\vec{Q},E)/\int dE S(\vec{Q},E)$,

$$\langle E(\vec{Q})^2\rangle = \frac{2}{3}S(S+1)\sum_{\vec{d}} J_{\vec{d}}^2[1-\cos(\vec{Q}\cdot\vec{d})], \qquad (11)$$

and assuming small momentum transfers q close to the magnetic Bragg peak and parallel to [100], we write

$$\lim_{q\to 0} E(q)^2 = S(S+1)\delta^2 J_1^2 q^2 = (\hbar c q)^2, \qquad (12)$$

with δ being the nearest-neighbor distance. Substituting a spin-wave velocity of 17.5 meV Å, derived from the dashed line in Fig. 16(a), and a bond length $\delta \sim 3.7$ Å (Table I), we obtain $J_1 = 1.6 \pm 0.3$ meV.

To derive values for the exchange constant between the triangles within the *ab* plane, we consider couplings (J_2 as indicated in Fig. 1) between triangles and use the following expression for an antiferromagnet:

$$E(H)^2 = 4S^2\left(\Delta^2 + J_2^2 \sin^2(2\pi H)\right). \qquad (13)$$

Here we have inserted an extra parameter Δ to take into account that we are not exactly at the magnetic-zone center for dispersion curves like those shown in Fig. 16(c) or for the presence of anisotropies as discussed above with regard to the spin waves along the (00L) direction. The solid curves in Figs. 16(a) and 16(c) are calculations using the above formula with $J_2 = 0.31 \pm 0.005$ meV.

The spin-wave dispersion around the zone boundary is illustrated in Fig. 16(b) and is sensitive to higher order (beyond nearest-neighbor) interactions between the triangles. While it is difficult to separate the modes along this direction, our results do show that there is relatively little dispersion along this direction in comparison to the energy values. This indicates a negligible next-nearest-neighbor interaction between the triangles, and such a scenario is represented by the flat line in Fig. 16(b).

In summary, based on the spin-wave dispersion curves in the *a-b* plane, we extract the following for the exchange interactions:

$$J_1 = 1.6 \pm 0.3 \text{ meV} \qquad (14)$$

$$J_2 = 0.31 \pm 0.05 \text{ meV}. \qquad (15)$$

A comparison between the experimental values and the spin-dimer calculation are presented in Table II. While J_2 is in reasonable agreement in the calculation, J_1 is considerably larger. We now compare the exchange parameters obtained for the Curie-Weiss temperature previously reported from the magnetization measurements as a check of the validity of the experimental derived exchange interactions.

VI. CURIE-WEISS TEMPERATURE

Based on our values for the exchange constants, we can obtain an estimate for the Curie-Weiss temperature (Θ_{CW}) using the formula

$$k_B\Theta_{CW} = \frac{1}{3}S(S+1)\sum_n J_n, \qquad (16)$$

where the sum is performed over nearest neighbors. The above result is derived from a mean-field approach and is based on the molecular field produced at a given site by the nearest neighbors and where the Hamiltonian can be reduced to a form $\sum_n \vec{S}_n \cdot \vec{H}_W$, where $\vec{H}_W$ is the molecular or Weiss field.[49] Owing to the fact that the magnetic structure in $Ba_3NbFe_3Si_2O_{14}$ is quite complex, it is not entirely clear how the Hamiltonian can be simplified to such a form to provide a direct value for the Curie-Weiss constant. Nevertheless, we can estimate the value as follows based on the spin-wave analysis described above and the number of nearest neighbors for a given Fe^{3+} ion:

$$\Theta_{\mathrm{CW}} = \tfrac{1}{3}S(S+1)\cdots \times 2 \times (J_1 + J_2 + J_3 + J_4 + J_5)/k_B \sim 170\ \mathrm{K}. \quad (17)$$

The terms for $J_{3,4,5}$ are quite rigorous, as there are two nearest neighbors. We have chosen to count J_1 twice and J_2 also twice, as each Fe^{3+} only has two neighbors coupled by each exchange pathway. The value obtained above is in reasonable agreement with the measured values of $\Theta_{\mathrm{CW}} = -173$ K and -190 K described in Refs. 18, 20 and 21. The comparison confirms the validity of our spin-wave analysis and the extracted parameters. It also confirms our assertion that a helical Heisenberg model is more appropriate for describing the physical properties of $Ba_3NbFe_3Si_2O_{14}$ rather than a model invoking a large Dzyaloshinskii-Moriya interaction term in the Hamiltonian.

VII. CONCLUSIONS

We have measured the spin fluctuations in $Ba_3NbFe_3Si_2O_{14}$ both at low temperatures and around T_N with the goal of understanding the ordering wave vector and the critical properties. We have found that the critical dynamics are consistent with those of other two-dimensional triangular magnets with a 120° magnetic structure. However, the critical wave vector and chirality are independent of temperature and the chiral nature of the diffuse scattering remains at temperatures well above T_N. Through an analysis of the structure using a spin-dimer calculation, we have followed a scheme where the exchange constants along the c axis are helical, with two different next-nearest-neighbor couplings. Using this and the fact that an XY picture seems appropriate, we derived the spin -waves for modes propagating along the c axis with the spins confined to the a-b plane and have derived the exchange constants. The values of the exchange constants are listed in Table II and compared with the values and compared with the values predicted from the spin-dimer and molecular orbital calculations.

The experimental values are in reasonable agreement with the spin-dimer calculation and reproduce the correct magnetic ordering wave vector and Curie-Weiss constants within error. These results indicate that the structural and magnetic chiralities are strongly coupled in $Ba_3NbFe_3Si_2O_{14}$ and that symmetric Heisenberg exchange is required for this. These results point to a unique magnetic system where the chirality is imposed by the nuclear structure and not the Dzyaloshinskii-Moriya interaction.

ACKNOWLEDGMENTS

We are grateful to A. Orszulik (ISIS) and H. Schneider (JCNS) for expert technical support throughout the experiments and to R. Coldea and R. Cowley for helpful discussions. We are indebted to J. Jensen for very helpful comments and suggestions. We are also grateful for grants from the EU-NMI3 Access Program for partial funding of this research. The work at Rugers was supported by the National Research Foundation of Korea (Grant No. KRF-2008-220-C00012).

APPENDIX: MEAN-FIELD DESCRIPTION OF THE SPIN WAVES

To model the spin waves, we start with the case of chains of coupled triangles [Fig. 1(b)] and, therefore, the Hamiltonian for isolated triangles weakly coupled along the c axis. Experimentally, we believe that this is a good starting point owing to the fact that the spiral propagation wave vector is along c and also the fact that the experimental dispersion within the a-b plane is substantially less complicated in comparison to the spin-wave dispersion along the [001] direction, as illustrated by comparing Figs. 12 and 14. This approach is also corroborated by the paramagnetic diffuse scattering presented earlier, which illustrated that the spin correlations along [001] were significantly stronger than those along [100]. Based on the coordination paths illustrated in Fig. 1, we pursue a model based on one nearest-neighbor exchange (J_4) and two next-nearest-neighbor exchanges ($J_{3,5}$). We therefore write the Heisenberg component of the spin Hamiltonian as

$$H_{H,i} = J_4 \vec{S}_i^a \cdot \vec{S}_{i+1}^a + J_3 \vec{S}_i^a \cdot \vec{S}_{i+1}^b + J_5 \vec{S}_i^a \cdot \vec{S}_{i+1}^c. \quad (A1)$$

The index i corresponds to different triangles along the c axis, and the indices a, b, and c describe the three different spins within a given isolated triangle. The interactions $J_{3,4,5}$ define the three different exchange pathways between two different triangles along a chain discussed above. The coupling between a and a spins on different triangles represents the nearest-neighbor interaction (J_4), and b and c spins correspond to next-nearest-neighbor interactions ($J_{3,5}$).

To obtain a dispersion for linear spin waves, we have imposed a ground state defined by the standard 120° structure within a triangle and a spiral along c, defined by the pitch angle α. Following previous spin-wave calculations for triangular antiferromagnets,[43] the transformations are represented by

$$S_j^{ax} = s_j^x \cos(j\alpha) - s_j^y \sin(j\alpha),$$
$$S_j^{ay} = s_j^y \cos(j\alpha) + s_j^x \sin(j\alpha),$$
$$S_j^{az} = s_j^z$$

for a spins;

$$S_j^{bx} = s_j^x \cos(j\alpha + 2\pi/3) - s_j^y \sin(j\alpha + 2\pi/3),$$
$$S_j^{by} = s_j^y \cos(j\alpha + 2\pi/3) + s_j^x \sin(j\alpha + 2\pi/3), \quad \text{(A2)}$$
$$S_j^{bz} = s_j^z$$

for b spins; and

$$S_j^{cx} = s_j^x \cos(j\alpha - 2\pi/3) - s_j^y \sin(j\alpha - 2\pi/3),$$
$$S_j^{cy} = s_j^y \cos(j\alpha - 2\pi/3) + s_j^x \sin(j\alpha - 2\pi/3),$$
$$S_j^{cz} = s_j^z$$

for c spins.

By symmetrizing the Hamiltonian and writing in terms of the new transformed coordinates s_i, the Heisenberg component of the Hamiltonian takes the form

$$H_{H,n} = \Gamma\left(s_n^x s_{n+1}^x + s_n^y s_{n+1}^y\right) + \Theta\left(s_n^z s_{n+1}^z\right), \quad \text{(A3)}$$

with

$$\Gamma = J_4 \cos(\alpha) + J_3 \cos(\alpha + 2\pi/3) + J_5 \cos(\alpha - 2\pi/3),$$
$$\Theta = J_3 + J_4 + J_5. \quad \text{(A4)}$$

This model therefore maps directly onto a Hamiltonian with XY symmetry. We note that this approach does not directly provide information on the exchange between $S = 5/2$ spins in a triangle that is expected to be the strongest interaction. However, the triangle-triangle coupling described by our model is crucial to understanding the spin waves and chirality along the c axis.

This approach follows closely the analysis applied to $Ba_2CuGe_2O_7$.[44,45] The main difference in our calculation is that we have imposed a chirality to the Hamiltonian through two different next-nearest-neighbor exchange constants $J_{3,5}$ instead of using a Dzyaloshinskii-Moriya interaction as required for $Ba_2CuGe_2O_7$. The Holstein-Primakoff transformations were then applied by writing the spin projections as $s_{n,m}^z = (-1)^{n+m}(S - a_{n,m}^\dagger a_{n,m})$, $s_{n,m}^x = (-1)^{n+m}(\sqrt{S/2})(a_{n,m}^\dagger + a_{n,m})$, and $s_{n,m}^y = i(\sqrt{S/2})(a_{n,m}^\dagger - a_{n,m})$ and keeping only terms quadratic in the ladder operators $a_{n,m}$ and $a_{n,m}^\dagger$. We then find the following for the Hamiltonian,

$$\frac{H_{H,n}}{S\Gamma} = (2a_n^\dagger a_n - a_n a_{n+1} - a_n^\dagger a_{n+1}^\dagger) + \cdots$$
$$- \frac{\gamma}{2}(a_n + a_n^\dagger)(a_{n+1} + a_{n+1}^\dagger) + 2\gamma a_n a_n, \quad \text{(A5)}$$

with $\gamma = \Theta/\Gamma - 1$. Based on this transformed Hamiltonian we can then define the A_q and B_q coefficients, and hence a dispersion relation, as

$$E(\tilde{L}) = S\Gamma\sqrt{A(\tilde{L})^2 - B(\tilde{L})^2}, \quad \text{(A6)}$$

where $A_{\tilde{L}}$ and $B_{\tilde{L}}$ are derived as

$$A(\tilde{L}) = 2(1+\gamma) - \gamma\cos(2\pi\tilde{L}),$$
$$B(\tilde{L}) = (2+\gamma)\cos(2\pi\tilde{L}). \quad \text{(A7)}$$

The mean-field description predicts three gapless modes at the incommensurate positions ($\tilde{L} = 1/2 \pm \alpha$) and at the commensurate position ($\tilde{L} = 1/2$). The modes are symmetrically located near the 1/2 position owing to our choice of the transformation of the spin coordinates listed above. To apply this model to our system where the triangles are ferromagnetically arranged, we apply the coordinate shift $\tilde{L} \to L + 1/2$.

While the model describes the dispersion of the two modes at $L = \pm\alpha$ (illustrated in Fig. 15 and by the highest energy mode in Fig. 16), it fails to describe the gapped response at the commensurate position and, also, the presence of the branch extending up to high energies. We therefore conclude that while the mean-field description provides a good description of the low-energy response, it fails at higher energies. It is possible that an extended treatment in terms of trimer clusters would be more appropriate for the spin waves in analogy to recent descriptions of $Cu_2Te_2O_5Cl_2$.[51] Nevertheless, the fact that we can accurately describe the lowest energy spin waves, the incommensurate wave vector, the Curie-Weiss temperature, and the spin-dimer calculation with our set of exchange constants provides significant credence to our description of the basic energy scales of this triangular magnet.

*cstock@nist.gov

[1] M. F. Collins and O. A. Petrenko, Can. J. Phys. **75**, 605 (1997).

[2] A. P. Ramirez, in *Handbook of Magnetic Materials*, edited by K. J. H. Buschow (Elsevier Science, Amsterdam, 2001), Vol. 13, pp. 423–520.

[3] H. Kawamura, Can. J. Phys. **79**, 1447 (2001).

[4] H. Kawamura, J. Phys. Condens. Matter **10**, 4707 (1998).

[5] P. W. Anderson, Mater. Res. Bull. **8**, 153 (1973).

[6] R. Coldea, D. A. Tennant, and Z. Tylczynski, Phys. Rev. B **68**, 134424 (2003).

[7] S. Nakatsuji, Y. Nambu, H. Tonomura, O. Sakai, S. Jonas, C. Broholm, H. Tsunetsugu, and Y. Qiu, and Y. Maeno, Science **309**, 1697 (2005).

[8] Y. Shimizu, K. Miyagawa, K. Kanoda, M. Maesato, and G. Saito, Phys. Rev. Lett. **91**, 107001 (2003).

[9] J. S. Helton, K. Matan, M. P. Shores, E. A. Nytko, B. M. Bartlett, Y. Yoshida, Y. Takano, A. Suslov, Y. Qiu, J.-H. Chung, D. G. Nocera, and Y. S. Lee, Phys. Rev. Lett. **98**, 107204 (2007).

[10] S.-H. Lee, H. Kikuchi, Y. Qiu, B. Lake, Q. Huang, K. Habicht, and K. Kiefer, Nat. Mater. **6**, 853 (2007).

[11] C. Stock, L. C. Chapon, O. Adamopoulos, A. Lappas, M. Giot, J. W. Taylor, M. A. Green, C. M. Brown, and P. G. Radaelli, Phys. Rev. Lett. **103**, 077202 (2009).

[12] M. Kenzelmann, A. B. Harris, S. Jonas, C. Broholm, J. Schefer, S. B. Kim, C. L. Zhang, S.-W. Cheong, O. P. Vajk, and J. W. Lynn, Phys. Rev. Lett. **95**, 087206 (2005).

[13] O. P. Vajk, M. Kenzelmann, J. W. Lynn, S. B. Kim, and S.-W. Cheong, Phys. Rev. Lett. **94**, 087601 (2005).

[14] D. Senff, P. Link, K. Hradil, A. Hiess, L. P. Regnault, Y. Sidis, N. Aliouane, D. N. Argyriou, and M. Braden, Phys. Rev. Lett. **98**, 137206 (2007).

[15]M. Kenzelmann, G. Lawes, A. B. Harris, G. Gasparovic, C. Broholm, A. P. Ramirez, G. A. Jorge, M. Jaime, S. Park, Q. Huang, A. Ya. Shapiro, and L. A. Demianets, Phys. Rev. Lett. **98**, 267205 (2007).
[16]T. Kimura, T. Goto, H. Sintani, K. Ishizaka, T. Arima, and Y. Tokura, Nature **426**, 55 (2003).
[17]M. Kitaura, K. Mochizuki, Y. Inabe, M. Itoh, H. Nakagawa, and S. Oishi, Phys. Rev. B **69**, 115120 (2004).
[18]H. D. Zhou, C. R. Wiebe, Y.-J. Jo, L. Balicas, R. R. Urbano, L. L. Lumata, J. S. Brooks, P. L. Kuhns, A. P. Reyes, Y. Qiu, J. R. D. Copley, and J. S. Gardner, Phys. Rev. Lett. **102**, 067203 (2009).
[19]L. L. Lumata, T. Besara, P. L. Kuhns, A. P. Reyes, H. D. Zhou, C. R. Wiebe, L. Balicas, Y. J. Jo, J. S. Brooks, Y. Takano, M. J. Case, Y. Qiu, J. R. D. Copley, J. S. Gardner, K. Y. Choi, and N. S. Dalal, and M. J. R. Hoch, Phys. Rev. B **81**, 224416 (2010).
[20]K. Marty, P. Bordet, V. Simonet, M. Loire, R. Ballou, C. Darie, J. Kljun, P. Bonville, O. Isnard, P. Lejay, B. Zawilski, and C. Simon, Phys. Rev. B **81**, 054416 (2010).
[21]K. Marty, V. Simonet, E. Ressouche, R. Ballou, P. Lejay, and P. Bordet, Phys. Rev. Lett. **101**, 247201 (2008).
[22]H. D. Zhou, L. L. Lumata, P. L. Kuhns, A. P. Reyes, E. S. Choi, N. S. Dalel, J. Lu, Y. J. Lo, L. Balicas, J. S. Brooks, and C. R. Wiebe, Chem. Mater. **21**, 156 (2009).
[23]G. Shirane, S. Shapiro, and J. M. Tranquada, *Neutron Scattering with a Triple-Axis Spectrometer* (Cambridge Press, Cambridge, 2002).
[24]C. Stock, W. J. L. Buyers, R. Liang, D. Peets, Z. Tun, D. Bonn, W. N. Hardy, and R. J. Birgeneau, Phys. Rev. B **69**, 014502 (2004).
[25]O. Scharpf and I. S. Anderson, Physica B **198**, 203 (1994).
[26]R. J. Christianson, Y. J. Wang, S. C. LaMarra, R. J. Birgeneau, V. Kiryukhin, T. Masuda, I. Tsukada, K. Uchinokura, and B. Keimer, Phys. Rev. B **66**, 174105 (2002).
[27]M. P. Zinkin, D. F. McMorrow, J. P. Hill, R. A. Cowley, J.-G. Lussier, A. Gibaud, G. Grubel, and C. Sutter, Phys. Rev. B **54**, 3115 (1996).
[28]V. P. Plakhty, W. Schweika, Th. Bruckel, J. Kulda, S. V. Gavrilov, L.-P. Regnault, and D. Visser, Phys. Rev. B **64**, 100402(R) (2001).
[29]O. Halpern and M. H. Johnson, Phys. Rev. **55**, 898 (1939).
[30]M. Blume, Phys. Rev. **130**, 1670 (1963).
[31]A. T. Moon, T. Riste, and W. C. Koehler, Phys. Rev. **181**, 920 (1969).
[32]W. Schweika, J. Phys. Conf. Ser. **211**, 012026 (2010).
[33]G. Shirane, R. Cowley, C. Majkrzak, J. B. Sokoloff, B. Pagonis, C. H. Perry, and Y. Ishikawa, Phys. Rev. B **28**, 6251 (1983).
[34]H. Kawamura, J. Appl. Phys. **63**, 3086 (1988).
[35]T. E. Mason, B. D. Gaulin, and M. F. Collins, Phys. Rev. B **39**, 586 (1989).
[36]B. D. Gaulin, T. E. Mason, M. F. Collins, and J. Z. Larese, Phys. Rev. Lett. **62**, 1380 (1989).
[37]M.-H. Wangbo, D. Dai, and H.-J. Koo, Solid State Sci. **7**, 827 (2005).
[38]H.-J. Koo, Inorg. Chem. **45**, 10743 (2006).
[39]B. I. Halperin and P. C. Hohenberg, Phys. Rev. B **188**, 898 (1969).
[40]C. Stock, S. Jonas, C. Broholm, S. Nakatsuji, Y. Nambu, K. Onuma, Y. Maeno, and J.-H. Chung, Phys. Rev. Lett. **105**, 037402 (2010).
[41]C. Stock, W. J. L. Buyers, Z. Yamani, Z. Tun, R. J. Birgeneau, R. Liang, D. Bonn, and W. N. Hardy, Phys. Rev. B **77**, 104513 (2008).
[42]B. Roessli, P. Boni, W. E. Fischer, and Y. Endoh, Phys. Rev. Lett. **88**, 237204 (2002).
[43]Th. Jolicoeur and J. C. Le Guillou, Phys. Rev. B **40**, 2727 (1989).
[44]A. Zheludev, S. Maslov, G. Shirane, I. Tsukada, T. Masuda, K. Uchinokura, I. Zalizynak, R. Erwin, and L. P. Regnault, Phys. Rev. B **59**, 11432 (1999).
[45]A. Zheludev, G. Shirane, Y. Sasago, N. Koide, and K. Uchinokura, Phys. Rev. B **54**, 15163 (1996).
[46]S. W. Lovesey, *Theory of Neutron Scattering from Condensed Matter* (Clarendon Press, Oxford, 1984).
[47]F. Moussa, M. Hennion, J. Rodriguez-Carvajal, H. Moudden, L. Pinsard, and A. Revcolevschi, Phys. Rev. B **54**, 15149 (1996).
[48]D. Senff, N. Aliouane, D. N. Argyriou, A. Hiess, L. P. Regnault, P. Link, K. Hradil, Y. Sidis, and M. Braden, J. Phys. Condens. Matter **20**, 434212 (2008).
[49]J. Jensen, private communication.
[50]J. B. Goodenough, *Magnetism of the Chemical Bond* (Interscience, London, 1963).
[51]P. C. Hohenberg and W. F. Brinkman, Phys. Rev. B **10**, 128 (1974).
[52]J. Jensen, Phys. Rev. B **79**, 014406 (2009).